Journal of Structural Geology 32 (2010) 1114–1124

Contents lists available at ScienceDirect

Journal of Structural Geology

journal homepage: www.elsevier.com/locate/jsg

Scale-invariance and self-organized criticality in migmatites of the southern Hualapai Mountains, Arizona

Chloë E. Bonamici*, Ernest M. Duebendorfer

School of Earth Sciences and Environmental Sustainability, Geology Program, Northern Arizona University, P.O. Box 4099, Flagstaff, AZ 86011-4099, USA

ARTICLE INFO

Article history:
Received 16 February 2010
Received in revised form
25 June 2010
Accepted 28 June 2010
Available online 19 August 2010

Keywords:
Migmatite
Melt-flow network
Scale-invariance
Self-organization

ABSTRACT

Whether or not melt-flow networks are scale-invariant may have broad implications for the understanding of the development of magmatic systems. Leucosome distributions in natural migmatite samples from the Hualapai Mountains, Arizona, are used to investigate the scaling characteristics of an inferred syndeformational melt-flow network. One-dimensional line and two-dimensional box-counting analyses yield distributions that are consistent with a scale-invariant relationship between the leucosome size and leucosome frequency. We infer from these results that the interactions of anatexis and deformation gave rise to a self-organized critical system in which melt distribution and melt movement were linked over a range of scales (at least millimeter- to meter-scale). We conclude that, even in metatexite migmatites volumetrically dominated by solid phases, melts can play an active role in determining the architecture of the melt-flow network. One implication of the envisioned self-organized critical system is the potential for rapid, large-scale melt coalescence and escape without long-term maintenance of a fully interconnected melt-flow network.

1. Introduction

Although most workers agree that migmatite terranes were sources for larger granitoid intrusions, they continue to debate the driving forces and mechanisms of melt coalescence and transfer between these anatectic zones and plutons (e.g., Mehnert, 1968; Petford et al., 1993; Brown et al., 1995a, b; Weinberg, 1999; Sawyer, 2001; Simakin and Talbot, 2001; Vanderhaeghe, 2009). The ultimate driving force of large-scale melt migration is buoyancy/gravitational instability (e.g., Clemens, 1998; Petford et al., 2000), but it remains unclear how efficient buoyancy alone is at driving melt coalescence locally within the anatectic zone, where the viscous properties and deformational states of solid-dominated migmatite (metatexite) exert a strong control on the location and interaction of melt segregations (e.g., Sawyer, 1994; Brown et al., 1995a, b; Holyoke and Rushmer, 2002; Vanderhaeghe, 2009). While plutons and batholiths testify to the efficacy of long-range, large-volume melt migration, predominantly local control of melt migration in the anatectic source region begs the question of how to affect the *focused and organized* extraction of melts from the source to the final site of emplacement.

Several studies document the rock record of melt-flow networks in migmatite terranes, which typically comprise leucocratic segregations (leucosomes) of variable shapes and sizes within a host of high-grade metamorphic rock (e.g., Brown and Solar, 1998; Brown et al., 1999; Vanderhaeghe, 1999; Ledru et al., 2001; Sawyer, 2001). Most workers infer that leucosomes represent crystallized partial melt segregations that interacted periodically through mass transfer (e.g., Brown et al., 1999; Marchildon and Brown, 2001). Various melt migration processes have been suggested from these natural examples, including pervasive grain-scale percolation (e.g., Sawyer, 1994; Laporte and Watson, 1995; Brown et al., 1999; Rabinowicz and Vigneresse, 2004), mesoscale diapirism (e.g., Weinberg and Podladchikov, 1994), dyking (e.g., Petford et al., 1993; Clemens, 1998), pervasive flow (Weinberg and Searle, 1998; Weinberg, 1999), and ductile fracturing (e.g., Eichhubl and Aydin, 2003; Brown, 2004), most of which are actuated and/or controlled by local stress and strain gradients (e.g., van der Molen, 1985; Brown et al., 1995a, b; Marchildon and Brown, 2001; Sawyer, 2001; Simakin and Talbot, 2001; Rabinowicz and Vigneresse, 2004).

Migmatite melt-flow networks are potentially useful analogues for magma transfer networks throughout the crust, provided that their spatial features can be scaled (Brown, 2001). Only a few studies have attempted to quantify the spatial distribution of

* Corresponding author. Present address: Department Geoscience, University of Wisconsin-Madison, 1215W. Dayton Street, Madison, WI 53706, USA.
E-mail addresses: bonamici@wisc.edu (C.E. Bonamici), ernie.d@nau.edu (E.M. Duebendorfer).

0191-8141/$ – see front matter © 2010 Elsevier Ltd. All rights reserved.
doi:10.1016/j.jsg.2010.06.019

natural migmatites and investigate the scaling properties of the melt-flow networks they represent. Different authors have applied subtly different techniques that assess different physical aspects of migmatites. Soesoo et al. (2004) found a power-law (scale-invariant) relationship between leucosome size and leucosome frequency over 2–3 orders of magnitude in Estonian drill core samples. In the most comprehensive study of its kind, Marchildon and Brown (2003) determined that migmatites of southern Brittany do not preserve evidence for a power-law distribution, either between the size and frequency of leucosomes (from 1-D analyses) or between the size and shape of leucosomes (from 2-D analyses). Tanner (1999) documents a power-law relationship in Bavarian migmatites over >1.5 orders of magnitude; however, as Marchildon and Brown (2003) point out, his analyses do not distinguish the signal associated with leucosome shape from that associated with leucosome frequency, making the resultant power-law relationship somewhat harder to interpret.

In this study, we find that stromatic (layered) migmatites of the southern Hualapai Mountains consistently show a scale-invariant relationship between the size and frequency of leucosomes both in one-dimensional line traverse analyses and two-dimensional surface analyses. The southern Hualapai migmatites differ from those previously investigated in that they generally contain a significantly higher percentage of leucosome (>65%) and yield significantly higher fractal dimensions ($D = 2.68–3.87$ in two-dimensional analyses). Because a single melting event is unlikely to produce >65% melt, we argue that the observed abundance of leucosome probably arose from temporal superposition of multiple melt-flow networks, each with a scale-invariant size–frequency relationship. The inferred tectonic history of the area (Bonamici and Duebendorfer, 2009) and outcrop-scale structures are consistent with diachronous melt-flow network creation and abandonment, and we argue that the preserved scale-invariant leucosome distribution signals an important, perhaps fundamental, mode of melt-flow network development in this system. We further discuss the possibility that the scale-invariant distribution indicates achievement of self-organized criticality (SOC) in this system and some associated implications for initiation and maintenance of through-going melt conduits in the crust.

2. Geologic background

The southern Hualapai Mountains study area (Fig. 1) is located within the proposed N-S-trending boundary zone between the isotopically distinct Mojave and Yavapai crustal provinces (Bennett and DePaolo, 1987; Wooden and DeWitt, 1991; Duebendorfer et al., 2006). The provinces were conjoined and then accreted to southwestern Laurentia during the Paleoproterozoic (Duebendorfer et al., 2001). Regionally, two phases of Paleoproterozoic deformation are distinguished: an early phase produced NNW-striking, moderately to gently dipping foliations and recumbent folds, and a later phase reoriented early fabrics to produce a NE-striking, steeply dipping foliation and upright folds (Karlstrom and Bowring, 1991; Albin and Karlstrom, 1991; Ilg et al., 1996; Duebendorfer et al., 2001). Early deformation occurred, at least in part, at 5–6 kbar and 650–750 °C (Ilg et al., 1996; Duebendorfer et al., 2001). Later deformation took place at similar temperatures but at reduced pressures of 3–4 kbar (Williams, 1991; Ilg et al., 1996; Hawkins et al., 1996; Duebendorfer et al., 2001).

The southern Hualapai Mountains study area comprises Paleoproterozoic basement exposed through a combination of Laramide uplift and high-angle normal faulting at the southwestern margin of the Colorado Plateau during Tertiary Basin-and-Range extension (e.g., Anderson, 1989). The area contains predominantly subhorizontally foliated granitoids and paragneisses with abundant

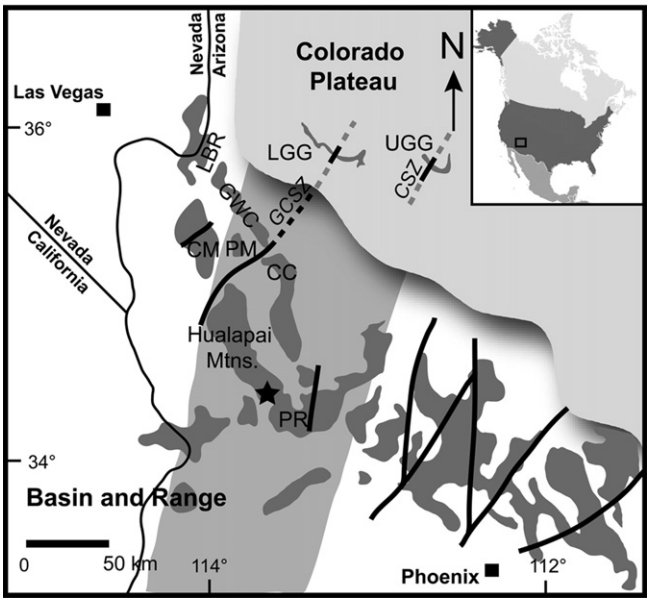

Fig. 1. Location map of northwestern Arizona modified from Duebendorfer et al. (2006) and Dumond et al. (2007). Darkest gray indicates exposures of Proterozoic rocks. Study area marked with bold star. Wide, lighter gray swath is the northeast-trending Mojave-Yavapai boundary zone of Wooden and DeWitt (1991). Heavy black lines are major faults or shear zones. CC-Cottonwood Cliffs; CM-Cerbat Mountains; CSZ-Crystal shear zone; GCSZ-Gneiss Canyon shear zone; GWC-Grand Wash Cliffs; LBR-Lost Basin Range; LGG-Lower Granite Gorge of the Grand Canyon; PM-Peacock Mountains; PR-Poachie Range; UGG-Upper Granite Gorge of the Grand Canyon.

textural and compositional evidence for pervasive partial melting. The following is a summary of structural and metamorphic data for the area, which are described in detail in Bonamici and Duebendorfer (2009).

2.1. Structures and deformation

The study area contains four types of deformational structures. The most prominent is a penetrative, gently dipping, variably striking foliation, defined in migmatitic units by well-developed compositional layering of leucosomes and melanosomes and in granitoids by grain-shape preferred orientation of feldspars, mica schistosity, or, more rarely, weak compositional layering (Fig. 2a). Lineations plunge gently to the east and west within the plane of foliation (Fig. 2b). Mesoscale inclined and recumbent folds are common in all rock types, and foliation is axial planar. Fold hinges plunge gently to the east and west and are parallel to lineations (Fig. 2b). North–south-striking, variably melt-filled, normal-sense shear bands both offset and sole into the foliation (Fig. 2c).

Based on the coplanar and colinear relations described above, we interpret foliation, lineations, and folds as codeformational structures accommodating *total finite* E-W subhorizontal extension and subvertical shortening; however, crosscutting, listric shear bands are compatible with finite E-W extension and subvertical shortening. We therefore infer that structures developed during a temporally and spatially related sequence of tectonic events with shear bands developing in the later stages of deformation and reactivating earlier-formed foliation, a common pattern of structural development in progressive simple shear (e.g., Platt and Vissers, 1980).

2.2. Pressure–temperature conditions of deformation

Macroscopic evidence for syndeformational melting includes well-developed migmatitic compositional layering, folded migmatitic

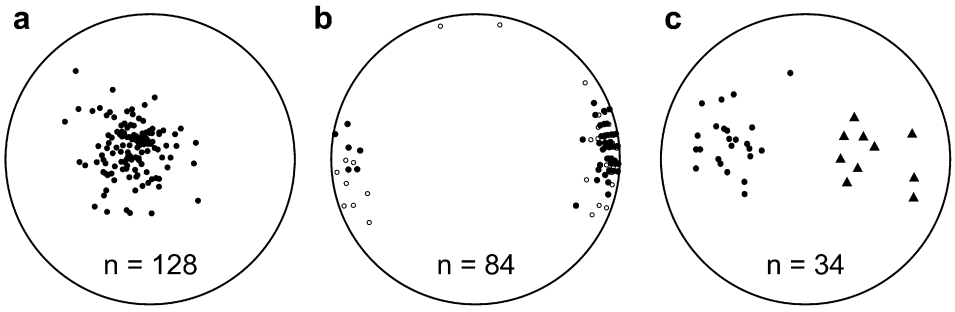

Fig. 2. Equal-area lower hemisphere nets showing structural data from the southern Hualapai Mountains. a) Poles to foliation planes. b) Lineations (filled) and fold hinges (open). c) Poles to conjugate normal-sense shear bands—closed circle are east-dipping bands and closed triangles are west-dipping bands.

layering, foliation-parallel leucosomes merging with compositionally and texturally identical crosscutting dikes, and some melt-filled shear bands. Microscopic evidence includes foliation-parallel preferred alignment of elongate euhedral feldspar crystals within leucosomes.

The typical metamorphic mineral assemblage of garnet and/or cordierite + biotite + sillimanite + K-feldspar + crystallized melt (in the absence of muscovite) indicates dehydration partial melting of a pelitic protolith at granulite facies conditions. Leucosomes are inferred to be crystallized melts on the basis of their felsic compositions, the presence of incongruent melting phases (garnet and cordierite), and preserved igneous microstructures, such as well-formed feldspar crystal growth faces (see Section 3). Thermobarometry constrains peak metamorphic conditions from early-grown garnet cores of 800 °C, 9.2 kbar and retrograde conditions of 670 °C, 4.5 kbar (Bonamici and Duebendorfer, 2009).

2.3. Tectonic interpretation and melt-deformation relations

Bonamici and Duebendorfer (2009) suggested that subhorizontal fabric formation and partial melting initiated during a period of crustal thickening and continued through a subsequent phase of near-isothermal decompression. In light of regional work, we interpret the southern Hualapai Mountains study area as exposing structures related to the Paleoproterozoic collision of the Mojave and Yavapai provinces and a succeeding episode of tectonic exhumation (Duebendorfer et al., 2001). The presence of melt must have affected crustal rheology during deformation and may have promoted tectonic exhumation following initial crustal thickening.

The similarity of metamorphic temperatures during thickening and exhumation and the evidence for the presence of melt during the development of all structures (early and late) lead us to conclude that partial melting and deformation interacted over an extended period of time. Thus, the southern Hualapai migmatites represent the preserved remains of a dynamic system in which deformation influenced the geometry of melt pathways and rates of melt migration, and melts influenced the spatial and temporal distributions of stress and strain.

3. Outcrop and thin section observations

Data for this study were gathered in and around Devil's Canyon, a drainage on the southwestern flank of the southern Hualapai Mountains, Arizona. Devil's Canyon provides rare, clean, stream-eroded, exposures in multiple orientations of foliation-parallel stromatic migmatites.

The migmatitic gneiss comprises alternating melanosomes and leucosomes with moderately to highly elongate lensoid shapes (collectively, stromata). Stomata are lensoid in outcrop surfaces, suggesting that both leucosomes and melanosomes have sheet-like geometries in three dimensions. Thicker leucosomes are laterally continuous over greater distances than thinner leucosomes. Melanosomes are less abundant and have a more limited range of thicknesses than leucosomes. Increasing melanosome thickness typically correlates with increasing leucosome thickness, with the thickest melanosomes generally adjacent to the thickest leucosomes. Centimeter-scale leucosomes commonly have interfingering geometries towards their terminations or along their boundaries that suggest merging of adjacent melt bodies (Fig. 3). Thicker leucosomes, those with thicknesses greater than 2–3 cm, display smoother boundaries but commonly contain melanosome schlieren (Fig. 4a). In many cases, melanosome schlieren define smaller, lensoid shaped zones of leucosome within larger leucosomes (Fig. 4b), suggesting that larger leucosomes result from the merging of smaller leucosomes.

Layer-parallel leucosomes connect with and feed into thicker, crosscutting dikes with similar compositions and textures (Fig. 5). Low-angle crosscutting dikes that wrap into parallelism or near-parallelism with gneissic layering are much more common than high-angle crosscutting dikes. In rare instances, high-angle crosscutting dikes are also deflected into near-parallelism with layering. The high relative abundance of stromatic leucosomes and low-angle crosscutting dikes compared with high-angle crosscutting dikes indicates that subhorizontal melt-flow predominated in this area.

Leucosomes are coarse grained and lack grain-shape fabrics at either the mesoscopic or microscopic scales. In thin section, many feldspars display well-formed crystal growth faces. Fine-grained quartz and feldspar commonly occupy grain triple junctions or

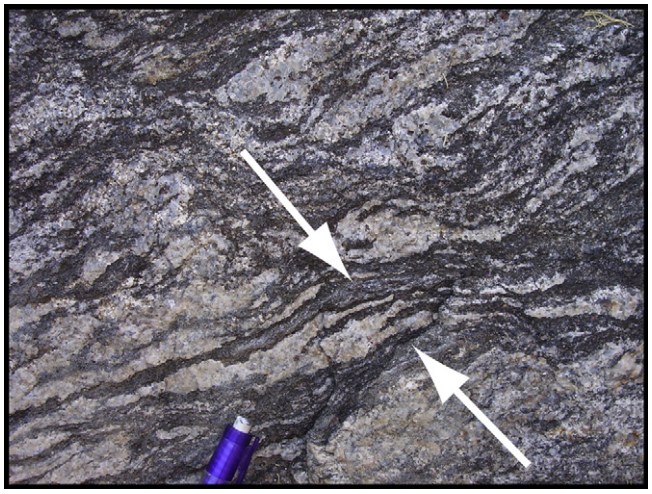

Fig. 3. Field photograph illustrating the common interfingering morphology of centimeter-scale leucosomes (between arrows). Subvertical, foliation-perpendicular outcrop surface. Pencil end for scale.

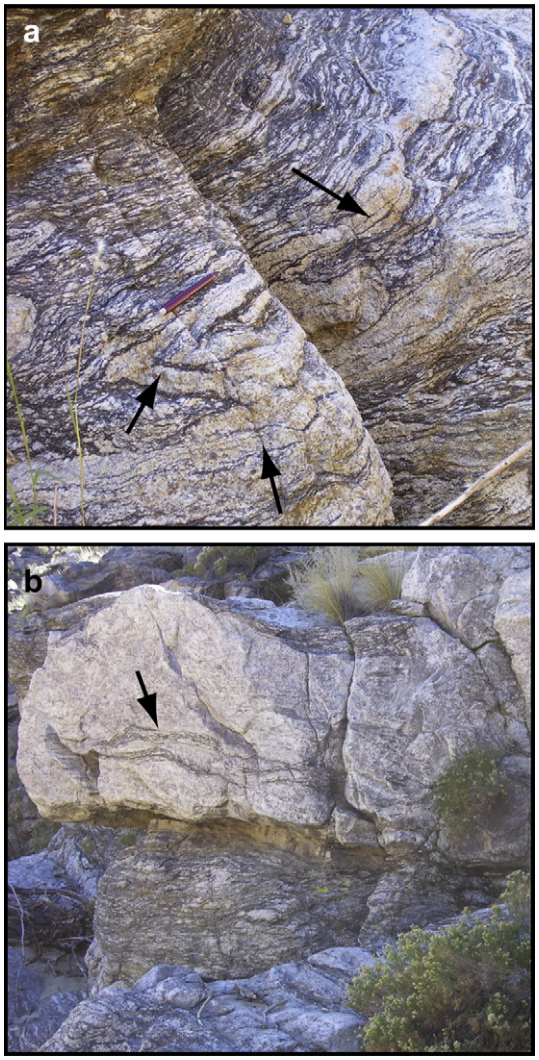

Fig. 4. Field photographs of melanosome schlieren in leucosomes. a) Layer-parallel leucosomes with abundant schlieren (arrows), some of which delineate smaller lensoid zones of leucosome within the larger leucosomes. These are interpreted to indicate that the larger leucosome body formed through coalescence of smaller leucosomes. Red pen for scale. b) Layer-parallel, meter-thick leucosome containing isolated melanosome schlieren (arrow).

appear as thin, mica-parallel grains that suggest crystallization from melt films along grain boundaries. We interpret such features as preserved igneous microstructures (cf., Vernon and Collins, 1988; Sawyer, 2001), which, despite their delicate forms, remain largely unmodified by subsolidus deformation.

4. 1-D line traverses

4.1. Data set

Because most leucosomes and melanosomes in the migmatitic gneiss are layered sheet-like bodies of widely varying, and often unknown, lateral extent, the most effective way to describe the spatial character of these stromata is by their layer-perpendicular thicknesses. Assuming a systematic scaling relationship between stromata layer-parallel length and stromata thickness, a three-dimensional stromatic body can be adequately and uniquely described by its one-dimensional thickness (Gillespie et al., 1993, 1999).

The major challenge to this scaling assumption arises from potential subsolidus modification of leucosome geometries by deformation. In the southern Hualapai Mountains, however, two lines of evidence suggest that leucosomes largely retain their suprasolidus dimensions. Although the migmatite package is clearly deformed, we see no field evidence for significant differential strain of any individual leucosome relative to another (e.g., strong strain gradients within the migmatite package). Instead, boudinaged leucosomes in lineation-parallel faces are mesoscopic evidence that strain was preferentially partitioned into biotite-rich melanosomes, while isotropic leucosome fabrics and preserved igneous microstructures are evidence that subsolidus leucosomes accumulated little internal strain. This observation does not, of course, preclude significant supersolidus deformation of the leucosomes. In combination, these observations suggest that leucosome morphology was fundamentally unchanged by post-crystallization deformation. The currently observed leucosome thicknesses are therefore a reasonable representation of supersolidus leucosome geometries.

Line traverses were performed at five sites to document leucosome and melanosome (stromata) thicknesses in the well-exposed main portion of the Devil's Canyon narrows. Following Marchildon and Brown (2003), a thin ribbon was taped to a subvertical outcrop perpendicular to compositional layering and the thickness of each transected melanosome was marked with a fine-tipped Sharpie marker (1 mm line thickness) on the ribbon (Fig. 6). In plots and figures, each traverse is designated by the pen color used to mark

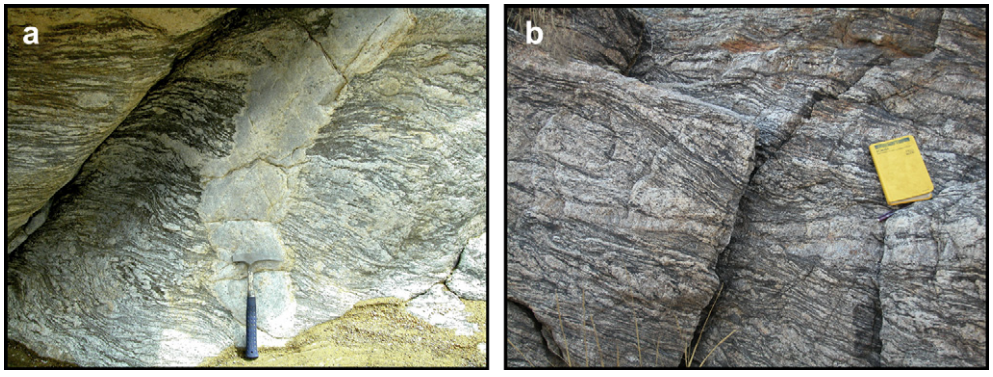

Fig. 5. Field photographs of crosscutting dikes. a) Rare dike at a high-angle to migmatitic compositional layering. Thin, layer-parallel leucosomes merge with the dike. Material in layer-parallel leucosomes and the crosscutting dike are compositionally and texturally continuous. Subvertical, foliation-perpendicular outcrop surface. Rock hammer for scale. b) Dike in a more common low-angle orientation with respect to layering. Low-angle dikes typically wrap into concordance with compositional layering. Subvertical, foliation-perpendicular outcrop surface. Field notebook for scale.

Fig. 6. Example of the method of gathering line traverse data. Green traverse in Figs. 9 and 10; total traverse length is 1669 mm. Melanosomes are marked on a ribbon taped to a subvertical, foliation-perpendicular surface. Leucosomes are represented by the intervening unmarked spaces. Field notebook (at very bottom of photo) for scale.

the ribbon, which served as an expedient means to distinguish the resulting ribbon records in notes, field photographs, and subsequent analyses. Although many leucosomes contain dispersed aggregates of melanosomal material, only those with elongate, layer-parallel morphologies and lateral continuity of greater than 1–2 cm were marked as representing melanosome stromata. Due to the size of the pen used and uncertainty in marking accuracy on an imperfectly flat surface, melanosomes thinner than 1 mm could not be resolved on the line traverses.

Comprehensive measurement and orientation data for each traverse are listed in Table 1. Traverse sites were closely spaced within the area of most cleanly exposed migmatitic gneiss in the Devil's Canyon narrows. All measured outcrop faces were perpendicular to foliation but variably oriented, with orientations ranging from E-W (lineation-parallel) to NNE-SSW, (close to lineation-normal). Traverse lengths were limited by heavy oxidation of gneiss above the modern channel level and precipitous ledges. Traverses ranged from 1.527 m to 2.680 m in total length. Each traverse recorded between 257 and 453 individual stromata. The thinnest stromata recorded were on the order of 1 mm, while the thickest (always leucosomes) approached 200 mm. The percentage of leucosome along each traverse was calculated as the ratio of the cumulative leucosome thickness to the total traverse length. Leucosome percentages for all traverses were tightly clustered at 65.7–67.8%, regardless of outcrop orientation (Table 1).

Following Gillespie et al. (1993), Gillespie et al. (1999), and Marchildon and Brown (2003), line traverse data were investigated in two main ways: 1) Cumulative leucosome thickness along the traverse and, 2) cumulative stromata frequency relative to stromata thickness. For all methods, leucosome thickness refers to the width of a leucosome measured along the traverse. Gillespie et al. (1993) originally developed this line counting method for use with faults, fractures, and veins, which have very small widths in comparison with their spacing. Because leucosomes have appreciable width, each leucosome is assigned a point location, which is here arbitrarily chosen as the center of the leucosome. For reference, the results of this study are compared with the synthetic, idealized distributions generated by Gillespie et al. (1993) (Fig. 7).

4.2. Cumulative thickness

Cumulative leucosome thickness curves for the five traverses show stepped profiles with several abrupt increases in total thickness alternating with ramp-like zones of more gradually increasing thickness (Fig. 8). Gradual ramp segments of the curve reflect continuous accumulation of thickness across zones of multiple, thin, closely spaced leucosomes, while large stepped increases indicate an abrupt, relatively large addition to cumulative thickness across a thick leucosome.

All cumulative leucosome thickness curves comprise a range of step sizes consistent with a power-law distribution of leucosome thicknesses. Immediately adjacent horizontal and vertical curve segments are generally not the same length, indicating a Kolmogorov-type (K-type) power-law distribution (Fig. 7b). This K-type distribution is consistent with the outcrop observation that melanosomes are always thinner than adjacent leucosomes and display a more limited range of thicknesses (see Section 3).

4.3. Cumulative frequency and thickness

Marchildon and Brown (2003) and Soesoo et al. (2004) adapted a method for determining the scale-dependence of mineralized veins (Gillespie et al., 1999; Loriga, 1999) to stromatic migmatites, such that the cumulative frequency of leucosome thickness is plotted against the range of thickness. These types of plots are

Table 1
Leucosome measurement data.

	UTM coordinates	Outcrop orientation	% leuc	Total length (mm)	Number of stroma (leuc/melan)	Average leucosome spacing (mm)	Fractal dimension (1D/2D)
orange	12 S 251255 E3832566	Subvertical; striking 080/260	66.67	1527	128/129	11.93	1.37/3.10
green	12 S 251268 E3832589	Subvertical; striking 020/200	67.82	1668.5	135/136	12.36	1.21/2.68
red	12 S 251263 E3832579	Subvertical; striking 060/240	65.70	1784	160/161	11.15	1.16/2.73
blue	12 S 251255 E3832554	Subvertical; striking 150/330	66.37	1684.5	226/227	7.45	1.84/3.86
purple	12 S 251274 E3832595	Subvertical; striking 030/210	67.62	2684	221/222	12.14	1.06/2.73

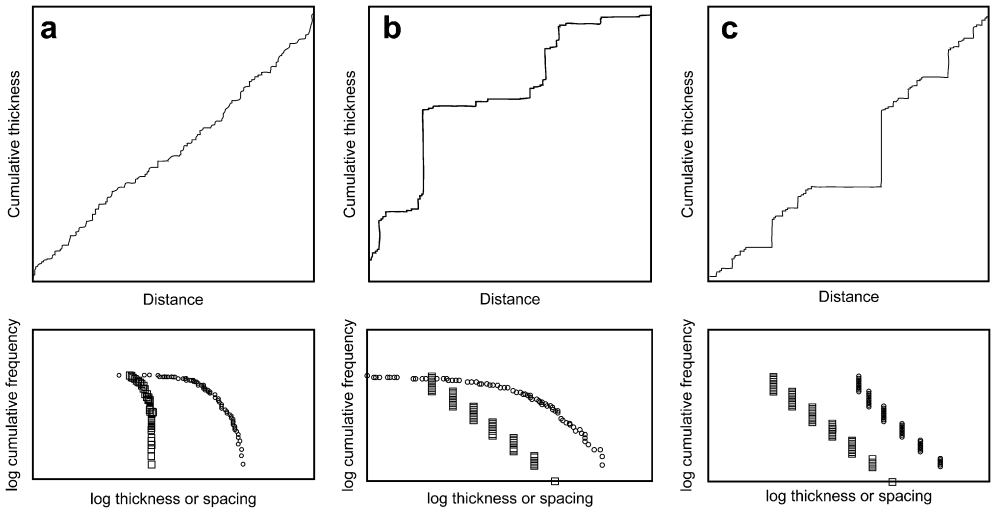

Fig. 7. Synthetically generated curves for a) random, b) Kolmogorov power-law, and c) fractal power-law distributions of vein cumulative thickness (top) and vein frequency (bottom). Open squares are thickness measurements. Open circles are spacing measurements. Adapted from Gillespie et al. (1999) to provide a visual comparison with results from this study.

a common way to test the relationship between the frequency of an event (i.e., a vein or leucosome or fault) and its size (e.g., Turcotte, 1997). A power-law relationship will manifest either as straight-line fractal-type or K-type distribution (Fig. 7b, bottom). A random distribution of thicknesses will produce a strongly concave downward curve with steepening slope towards greater thicknesses (Fig. 7c; Gillespie et al., 1993; Marchildon and Brown, 2003).

Cumulative frequency is calculated as the number of leucosomes with thickness greater than any particular thickness. On a log–log plot, a power-law distribution of thickness and/or spacing will produce a straight-line over greater than one order of magnitude described by

$$N_t = Ct^{-D}$$

where N_t is the number of leucosomes of a certain thickness t, D is the slope of the line (also called the fractal dimension), and C is a constant of proportionality (Turcotte, 1997; Gillespie et al., 1999).

All five traverses exhibit broadly concave downward cumulative frequency-versus-thickness curves (Fig. 9). Leucosome thickness curves show a moderate, stepping increase in slope toward greater thicknesses and decreasing slope toward lower thicknesses. The intervening segments of the leucosome curves between higher and lower thicknesses, however, show good correlation with modeled, straight-line, power-law curves with $D = 1.06–1.84$, though the

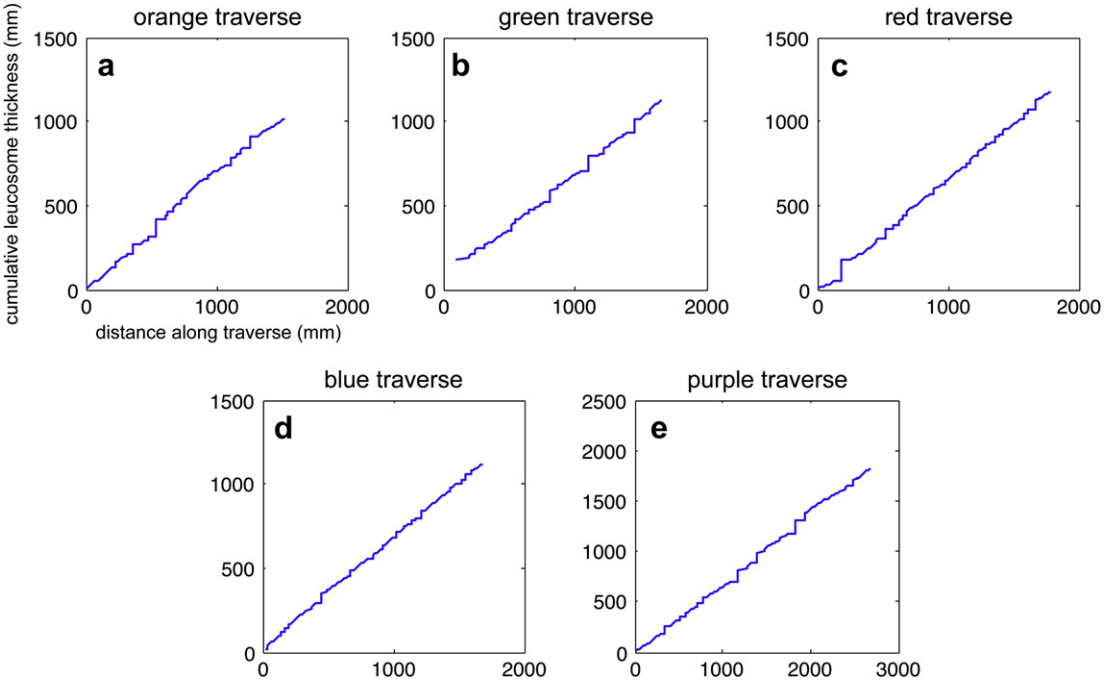

Fig. 8. Staircase plots of cumulative leucosome thickness versus distance along traverses. Horizontal curve segments represent the distance between leucosome centers. Vertical segments represent the addition of a leucosome thickness at the location of the leucosome center. Curves are most consistent with Kolmogorov-type power-law behaviour in which "steps" display a range of sizes and immediately adjacent horizontal and vertical curve segments have different lengths (cf. Fig. 7).

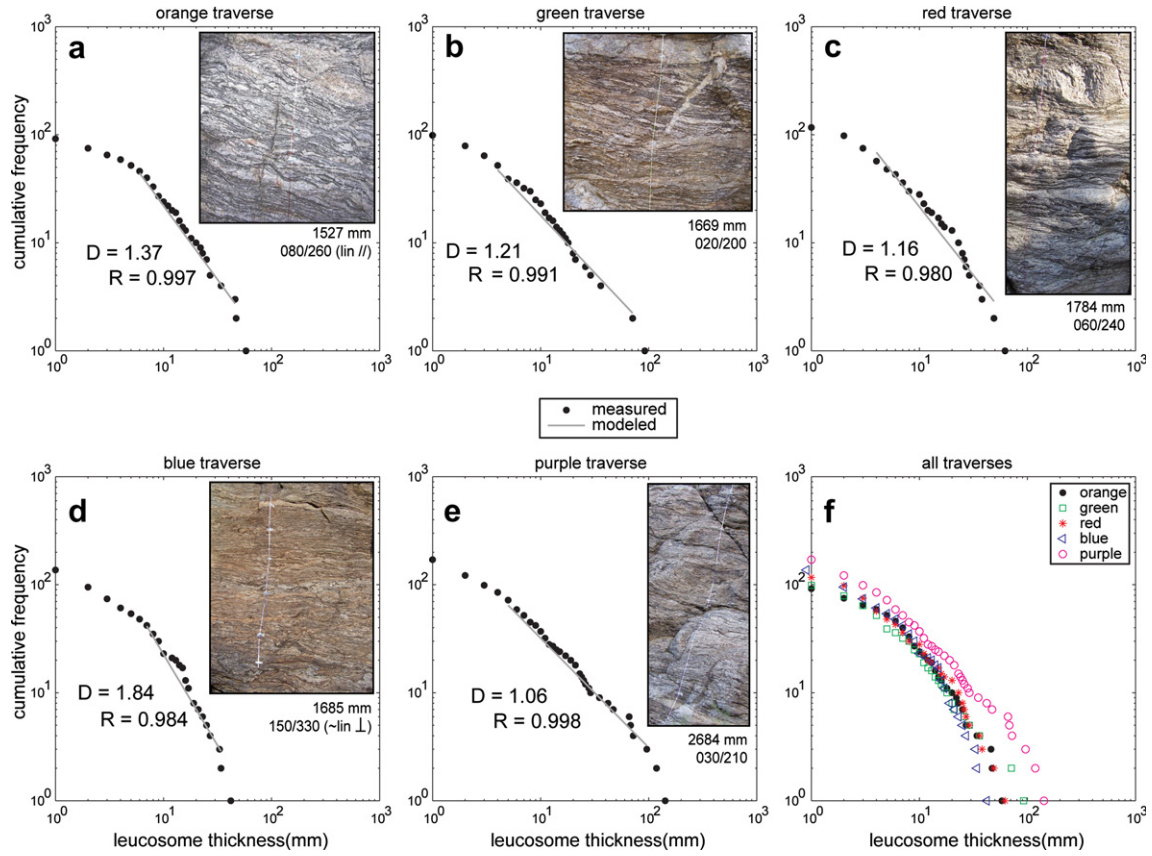

Fig. 9. Log–log plots of cumulative frequency-versus-leucosome thickness. Closed circles indicate the number of leucosomes with thickness greater than or equal to the thickness plotted on the ordinate. Thin lines are least-squares fit power-law curves generated through matrix inversion of the central range of values from each traverse. Insets of photographs of line traverse outcrops. Traverse length in millimeters and strike of each outcrop surface shown below inset photographs. Fractal dimension D (slope of the model curve) and correlation coefficient R shown for each model curve. The lower righthand plot shows cumulative frequency data for all traverses for comparison.

upper value of 1.84, which comes from the blue traverse, is anomalously high (Fig. 9d). *D*-values for the other four traverses range between 1.06 and 1.37. Despite differences in total traverse length and total number of leucosomes measured per traverse, frequency curves are tightly clustered for thicknesses between one and thirty millimeters (Fig. 9f). Above thirty millimeters thickness, curves diverge substantially but retain similar, stepping morphologies.

Cumulative frequency-versus-leucosome thickness curves are consistent with K-type power-law distributions and scale-invariant behaviour over 1.0–1.5 orders of magnitude. Several workers have recognized that these broadly concave distributions are governed by power-law relationships with fractal dimensions equal to the slope of the central straight-line segments (e.g., Bak et al., 1988; Turcotte, 1997; Loriga, 1999; Bons and van Milligen, 2001; Bons et al., 2004). Turcotte (1997) terms such data sets "statistical fractals" to emphasize that the underlying data define an imperfect but statistically meaningful power-law distribution. In this study, statistical analyses of cumulative frequency curves confirm that the central segment of each curve is essentially and significantly linear. Central curve segments, excluding 2–4 data points at the lowest and highest thicknesses (greatest measurement error), were fitted using least-squares linear regression. Pearson's correlation coefficient between modeled (fit) lines and data curves are 0.980–998. Bootstrapping of the correlation coefficients yields tight, unimodal distributions with distinct peaks at the mean values for all curves, verifying that coefficients accurately represent the significance of the correlation. Kolmogorov–Smirnov statistics that test whether a given distribution represents discrete and limited sampling of a known continuous distribution, show that cumulative frequency curves and their respective modeled regression lines could be generated from the same underlying distribution at the 95% confidence level.

Deviations from a straight-line power-law distribution toward the ends of each cumulative frequency curve can be, at least in part, attributed to known measurement limitations. The downward deflection towards greater cumulative frequency likely reflects the ~1 mm lower limit of resolution for this study and the choice of size categories for analyzing data. As noted above, the pen used for marking stromata on line traverses imposes a 1-mm lower limit on resolution. Because stromata thicknesses were rounded to the nearest millimeter and data were sorted into 1-mm size categories for plotting, sorting of thin stromata (<10 mm) was more affected by small errors in marking or measuring thicknesses than sorting of thicker stromata. The stairstep morphology of the curves towards greater thickness may be symptomatic of an insufficiently large dataset (Gillespie et al., 1993). In the case of this study, line traverses were likely too short to fully characterize the distribution of the thickest leucosomes, which were observed to be on the order of a meter elsewhere in the study area but were not encountered on any of the traverses (Fig. 4b).

Comparing all traverses, the divergence of leucosome thickness curves towards greater thickness correlates with total traverse length (Fig. 9f). The thickest leucosomes were encountered along the longest traverse; maximum leucosome thickness and spacing were less for shorter traverses. The four shorter traverses show no systematic relation between traverse length and maximum leucosome thickness, but the length range amongst these shorter traverses is 257 mm, while the longest traverse exceeds the next

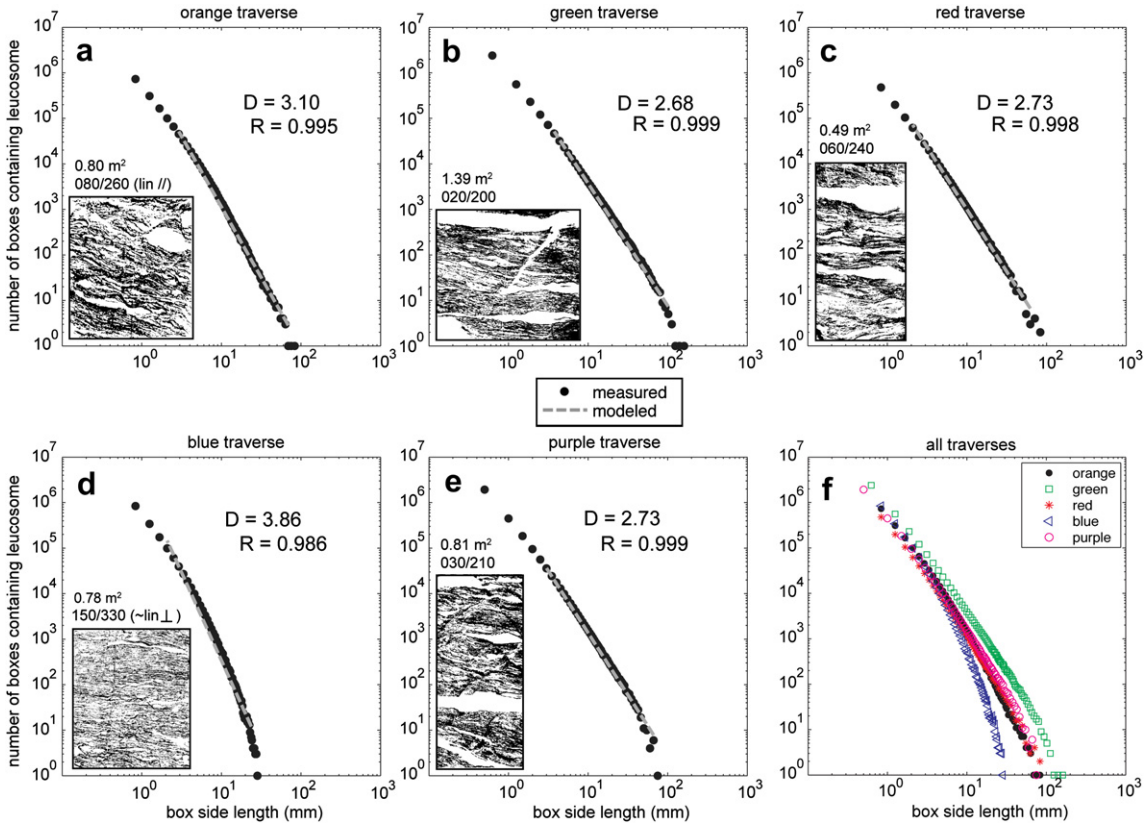

Fig. 10. Box-counting results for images of the same outcrops on which line traverse data were collected. Closed circles indicate the number of boxes containing only leucosome for a given box side length. Dashed lines are least-squares fit power-law curves generated through matrix inversion of the central range of values from each traverse. Insets of binary images used for box-counting. See Fig. 9 for traverse lengths and outcrop orientations. Fractal dimension D (slope of the model curve) and correlation coefficient R shown for each model curve. The lower righthand plot shows cumulative frequency data for all traverses for comparison. Compare with Fig. 9.

longest traverse by 900 mm. The total number of stromata measured per traverse may also correlate with higher maximum leucosome thicknesses; however, because the blue traverse, which records the greatest number of stromata, shows the smallest maximum stromata thicknesses, the correlation of traverse length with maximum stromata thicknesses appears to be more robust for this dataset. This correlation suggests that leucosomes may show a scale-invariant distribution through higher orders of magnitude than observed in this study.

5. 2-D image analyses

5.1. Data set

Following Tanner (1999), the two-dimensional spatial distribution of leucosomes was assessed through image analysis of photographs of migmatite outcrops. Although stromatic migmatites lend themselves to one-dimensional analysis as discussed above, two-dimensional analysis offers a more robust approximation of leucosome volumes and provides an independent check on the scaling assumptions inherent in the one-dimensional line traverse analyses.

Each outcrop measured in the 1-D line traverses discussed above was also photographed. All photographed outcrop surfaces are approximately planar with minor roughness. Two photos were adjusted in Image SXM to lessen shadow effects. Images were not corrected for perspective distortion prior to analysis because all were taken at a nearly 90° angle to the surface. All surfaces were photographed perpendicular to foliation. Total area analyzed for each outcrop ranged from 0.49 to 1.39 m^2.

5.2. Box-counting cumulative frequency

The box-counting method measures the frequency of a phenomenon at a given scale of observation (e.g., Turcotte, 1997). If the frequency and the scale of observation are related by a power-law such that

$$N_d = kn^{-D}$$

where N_d is the number of boxes containing the phenomenon of interest, n is the box side length, D is the fractal dimension (or slope of the power-law curve), and k is a constant (Turcotte, 1997; Tanner, 1999), then the phenomenon is scale-invariant. This is the two-dimensional equivalent of the cumulative frequency method discussed in the line traverse section.

Original color photographs were loaded into Image SXM, median filtered, adjusted for shadows, thresholded, and transformed into binary images, with white pixels representing leucosome and black pixels representing melanosome. Binary images were then loaded into MatLab, divided into boxes, and the number of boxes containing *only* leucosome was counted (MatLab code, Supplementary files). The box-counting was repeated for boxes of several different sizes, with box sides ranging from less than 1 mm up to 100s of mm in length.

All analyzed images of Hualapai migmatitic gneiss yield broadly concave curves (Fig. 10). Modeled fractal dimensions for curves are $D = 2.68–3.86$. This downward concavity is similar to, though subtler than, the downward concavity displayed by line traverse cumulative frequency curves (cf. Fig. 9). As with the one-dimensional analysis, the two-dimensional curve likely represents a Kolmogorov-type distribution, the imperfect shape of which reflects

limited and random sampling of a larger data set: the probability of adequately sampling very low and very high frequency events (very small and very large leucosomes) is inherently lower than the probability of sampling moderate frequency events. Deviations from perfect fit toward high box number may reflect pixel resolution, and because pixel resolution of images is substantially better than measurement resolution on line traverses (~1 mm), the deviation from linear is much smaller in the 2-D than in the 1-D case. Deviation at high box number (small box size) may also reflect uncorrected shadows in the image, which artificially increase the number of black (melanosome) boxes in some parts of the image.

As in the 1-D case, statistical analyses show the box-counting curves to be significantly linear. Curves generated through image analysis and least-squares fit power-law curves (models) show strong correlation coefficients of $R^2 = 0.986–999$. Bootstrapping of correlation coefficients reveals unimodal distributions with distinct peaks; mean correlation coefficients reported therefore accurately represent the significance of the correlation. Kolmogorov–Smirnov statistical tests indicate that measured and modeled distributions may be derived from the same underlying distribution at the 95% confidence level (MatLab code, Supplementary files).

5.3. Methodological comparison

Bons et al. (2004) point out that the scale-dependence or scale-independence of a 3-D system can only be truly determined on the basis of the volumetric distribution of phases. Marchildon and Brown (2003), in implementing the box-counting method, counted only those boxes containing both leucosome and melanosome, which, in effect, measured the perimeter length of leucosomes. This approach, in which leucosome perimeter length is a proxy for leucosome volume, is sensitive to patterns of leucosome distribution in physical space but does not necessarily identify patterns of leucosome distribution in frequency space (i.e., the probability of encountering a leucosomes of a particular size). In contrast, we count boxes containing *only* leucosome. Whereas box-counting of leucosome perimeters measures the shape of leucosomes or roughness of leucosome boundaries, box-counting of leucosome area determines the occurrence of leucosomes of a given areal extent or greater, regardless of perimeter shape. For this study, this method has the advantage of being a direct 2-D counterpart to 1-D cumulative frequency analyses, which quantify the relationship between leucosome size (thickness) and leucosome frequency. Our analyses do not address the relationship between the size of a leucosome and its shape because stromatic leucosomes are essentially planar objects in three dimensions (Tanner, 1999) and therefore will not show significant variations in perimeter roughness.

In this study, we chose not to evaluate changes in the slope of the box-counting curves as Marchildon and Brown (2003) did. Because distributions are clearly statistical fractals and likely to be K-type power-law distributions, slope variations are inherent and expected. Also, any slope calculation for a curve defined by discrete data points requires an averaging scheme over segments, and the calculated value of the slope for a given segment will depend strongly on the particular scheme employed.

5.4. Comparison of 1-D and 2-D data

One-dimensional and two-dimensional cumulative frequency data, although generated through two different methods, show strong similarities of both general shape and individual detail, and we therefore suggest that the data sets represent independent lines of evidence for a scale-invariant leucosome distribution. All curves have the same broad downward concavity with approximately straight-line central segments and statistically robust power-law distributions over 1.0–2.0 orders of magnitude. Departures from the power-law trend of the central segments are greatest at for small leucosomes – those that are very thin in one dimension or have small area in two dimensions. Although less pronounced in the 2-D frequency curves, both data sets show the small stairstep-like discontinuities at the high end of the size distribution that are characteristic of undersampling of large leucosomes (Gillespie et al., 1999). This stairstep effect is most pronounced for the red (Figs. 9c, 10c) and purple traverses (Figs. 9e, 10e) in both data sets. Also, in both data sets, the blue traverse has the most compressed range of leucosome sizes and, consequently, the highest fractal dimensions. Thus, although the 1-D dataset is somewhat imperfect and the interpretation of its origin as fractal is not entirely obvious, it captures the same spatial patterns represented in the 2-D dataset, which is derived from the same outcrops and has a much clearer affinity to the expected straight-line fractal distributions.

6. Discussion

6.1. Melt-flow network superposition

Given the coherency of fabrics and structures, it is unlikely that all leucosomal material currently observed in the migmatitic gneiss, which exceeds 65% in line traverses, was molten at the same time. Rather, leucosomes probably represent the superposition of remnants of more than one generation of melt-flow network. Such superposition is unlikely to have been strictly volumetrically linear: some melt conduits may have drained and collapsed (e.g., Brown et al., 1999; Guernina and Sawyer, 2003), while others froze with melt *in situ* and were partially or entirely obscured by subsequent migrating melt, and yet others were reopened by later phases of melt migration (Vigneresse and Burg, 2000; Bons et al., 2004). Unraveling the contributions of several temporally disparate melt-flow networks to the current leucosome distribution is enormously complex; however, we argue that the generation of a non-random, power-law signal through the non-linear superposition of multiple random signals requires geologically unreasonable coincidences (Supplementary files). Thus, at least some, if not most or all of the superimposed melt-flow networks contributed a power-law signal to produce the total, finite power-law signal detected in this study.

In fact, the relatively high fractal dimensions obtained for both 1-D (1.06–1.84) and 2-D (2.68–3.86) analyses may be symptomatic of *temporal* superposition of scale-invariant melt-flow networks. Fractal dimensions reflect the dimensionality of the feature being measured, such that linear features tend to be associated with fractal dimensions of ~1, planar features with ~2, and volumetric features with ~3. We therefore expect the line traverses to yield *D*-values around 1 and image box-counting to yield *D*-values around 2. Systematically greater than-expected *D*-values suggest dimensional effects beyond the spatial dimensions of leucosomes.

6.2. Self-organized criticality (SOC)

Self-organization is known to arise in multicomponent, dynamic, disequilibrium systems (Bak et al., 1988; Jensen, 1998; Sornette, 2000). A system is recognized as having attained self-organized criticality when it evolves toward and consistently returns to a particular critically stable state, regardless of the system's initial conditions or the details of systemic perturbations (Bak et al., 1988). The classic example of SOC is a sand pile at the angle of repose; any addition of sand oversteepens its slopes and drives the pile into an unstable configuration, but it always evolves through avalanching back toward the angle of repose (Bak et al., 1988). A more complex geologic example is expressed in critical

taper theory, where propagation of a fault-bounded wedge occurs only when the wedge achieves a particular critical angle. Wedges fluctuate about the critical taper angle for hundreds of thousands to tens of millions of years through the interaction of several mechanisms, including internal deformation of the wedge, migration of the basal detachment, and variations in fluid pressure along the bounding faults (e.g., Dahlen, 1990; DeCelles and Mitra, 1994).

Because the fundamental driving forces and many of the mechanisms of SOC are as yet unknown, SOC is essentially an empirically determined state. Characteristically, self-organized critical systems develop scale-invariant spatial and temporal phenomena (Bak et al., 1988; Turcotte, 1997). Thresholded response to changing conditions and avalanching (decoupling between the magnitude of perturbation and response) are some of the most common behaviours (Jensen, 1998; Sornette, 2000). Active systems that display these features and behaviours are considered to be in a state of self-organized criticality.

The evidence of self-organization and SOC in an *extinct* system necessarily and almost exclusively hinges on the preserved spatial features of the system and such system behaviours as can be interpreted from those preserved spatial features. Several aspects of the geologic record of anatectic systems suggest the potential for SOC. Tanner, (1999), Soesoo et al. (2004), and this study find evidence for scale-invariant size distributions of leucosomes. High fractal dimensions reported in this study also point to temporal scale-invariance of the melt-flow network architecture as represented by leucosome size distributions. Textural evidence for coalescence of mesoscale partial melts (Figs. 3 and 5; Brown, 2004) and the common spatial association of migmatites with granitic plutons (Brown and Solar, 1998) have been used to suggest that pluton emplacement occurs by rapid, large-scale melt escape (avalanche) when small melt bodies are present in sufficient number or achieve a favorable spatial arrangement (surpass a threshold) (Bons et al., 2004; Brown, 2004).

Analogue (Bons and van Milligen, 2001) and numerical models (Vigneresse and Burg, 2000; Bons et al., 2004) of melt migration demonstrate the spontaneous development of SOC, such that both the frequency and the escape time interval, as functions of the size of escaping melt batches, are scale-invariant. Important factors influencing the development of SOC in these models included melt mobility and the volume of the escaping melt batch relative to the volume of the melt batches remaining *in situ* (Bons et al., 2004). Deformation plays a key role in determining melt mobility by producing stress and strain gradients along which melts migrate (e.g., Sawyer, 1994; Brown et al., 1995a, b; Weinberg et al., 2009); therefore, deformation favors the development of SOC in anatectic systems (Vigneresse and Burg, 2000; Bons et al., 2004). A low escape-volume threshold hinders the development of SOC by decreasing the range of melt batch sizes and the range of frequencies of melt escape episodes to less than some critical threshold (Bons and van Milligen, 2001; Bons et al., 2004).

We suggest that the scale-invariant frequency distribution and the inferred self-organized criticality of southern Hualapai migmatites reflects a combination of deformation-imposed melt pathway anisotropy and infrequent melt extraction. Direct upward migration of melts was likely inhibited by the subhorizontal orientation of most flow paths (Fig. 6). Efficient upward migration would require extraction and transfer of melts from the source locations along low-angle conduits to a few, relatively large high-angle conduits. Inefficient melt escape, on the other hand, would result in retention of much of the melt near the source, where it could interact locally to form a wide range of melt batch sizes (Bons et al., 2004).

Finally, many authors have clearly demonstrated feedbacks between deformation-induced pressure gradients that drive melt migration and melting that localizes deformation (e.g., Weinberg and Mark, 2008), but evidence for self-organized critical behaviour in metatexite migmatites raises the possibility that melts themselves played an *active* role in influencing the morphology of the melt-flow network. This contrasts with a common model, both explicitly and implicitly applied by many workers, in which the loci and geometries of coalesced melt in metatexites are largely *passive* responses to preexisting and/or deformation-imposed anisotropies of the host-rock (e.g., Van der Molen, 1985; Hand and Dirks, 1992; Brown et al., 1995a, b; Vanderhaeghe, 2001; Vigneresse and Tikoff, 1999; Sawyer, 2001; Holyoke and Rushmer, 2002; Brown, 2004). Passive models invoke a solid host-rock framework that contains and constrains melt. In passive models, interaction between melt bodies requires direct contact through mass transfer, and melt migration occurs through a physically connected series of conduits and pathways from the zone of melt generation to the ultimate site of melt emplacement (Petford et al., 1993; Vigneresse and Burg, 2000; Brown, 2004). Instead, if SOC arises due to melt-deformation interactions, melt migration at one location may reflect spontaneous reorganization of the system in response to addition or movement of melt in any other part of the system, regardless of whether the melts are in direct physical contact; therefore, long-term maintenance of a fully connected flow path is not necessarily required to transfer melt from anatectic zones to emplacement sites (also see Bons et al., 2004). In other words, SOC suggests a potential mechanism to propagate perturbations arising from local melt-deformation interactions to the length-scale of the anatectic zone. SOC is thus likely to be both compatible with and complementary to passive melt migration models.

7. Conclusions

One- and two-dimensional analyses of stromatic migmatites show scale-invariant leucosome frequency distributions over 1–2 orders of magnitude. Combined with outcrop-scale observations of leucosomes these results suggest that the southern Hualapai migmatites represent a self-organized critical system developed through the interaction of deformation and partial melting. Self-organized criticality indicates that melts, even in solid-dominated metatexite type migmatites, play an active role in determining the spatial and temporal configuration of the melt-flow network and that such networks are potentially capable of discharging large melt volumes without long-term maintenance of a fully interconnected system of melt conduits.

Acknowledgements

We wish to thank Tom Hoisch and Mary Reid for comments on early drafts of this study. We also thank Sandy Cruden, Roberto Weinberg, Holger Stüniz, and David Tanner for helpful and thought-provoking reviews of this manuscript. We are grateful to the owners of the Bar S Ranch for allowing us access to the study area. This study was supported by GSA graduate student research grant to C. Bonamici, the Tom and Rose Bedwell Earth Sciences Award (NAU), and the Friday Lunche Clubbe.

Appendix. Supplementary data

Supplementary data associated with this article can be found in the online version, at doi:10.1016/j.jsg.2010.06.019

References

Albin, A.L., Karlstrom, K.E., 1991. Orthogonal Proterozoic fabrics in northwestern Arizona: multiple orogenic events or progressive deformation during continental assembly. In: Karlstrom, K.E. (Ed.), Proterozoic Geology and Ore Deposits of Arizona. Arizona Geological Society Digest, vol. 19, pp. 67–84.

Anderson, P., 1989. Proterozoic plate tectonic evolution of Arizona. In: Jenney, J.P., Reynolds, S.J. (Eds.), Geological Evolution of Arizona. Arizona Geological Society Digest, vol. 17, pp. 17–56.
Bak, P., Tang, C., Wiesenfeld, K., 1988. Self-organized criticality. Physical Review A 38, 364–374.
Bennett, V.C., DePaolo, D.J., 1987. Proterozoic crustal history of the western United States as determined by neodymium isotopic mapping. Geological Society of America Bulletin 99, 674–685.
Bonamici, C.E., Duebendorfer, E.M., 2009. Gravitational collapse of a Paleoproterozoic orogen, southern Hualapai Mountains, Arizona. Precambrian Research 175, 35–50.
Bons, P.D., Arnold, J., Elburg, M.A., Kalda, J., Soesoo, A., van Milligen, B.P., 2004. Melt extraction and accumulation from partially molten rocks. Lithos 78, 25–42.
Bons, P.D., van Milligen, B.P., 2001. New experiment to model self-organized critical transport and accumulation of melt and hydrocarbons from their source rocks. Geology 29, 919–922.
Brown, M., 2001. Crustal melting and granite magmatism: key issues. Physics and Chemistry of the Earth: Part A, Solid Earth and Geodesy 26, 201–212.
Brown, M., 2004. The mechanism of melt extraction from lower continental crust of orogens. Transactions of the Royal Society of Edinburgh, Earth Sciences 95, 35–48.
Brown, M., Averkin, Y.A., McLellan, E.L., 1995. Melt segregation in migmatites. Journal of Geophysical Research B8 100, 15655–15769.
Brown, M.A., Brown, M., Carlson, W.D., Denison, C., 1999. Topology of syntectonic melt-flow networks in the deep crust: inferences from three-dimensional images of leucosome geometry in migmatites. American Mineralogist 84, 1793–1818.
Brown, M., Rushmer, T., Sawyer, E.W., 1995. Introduction to special section: mechanisms and consequences of melt segregation from crustal protoliths. Journal of Geophysical Research B 100, 15551–15563.
Brown, M., Solar, G.S., 1998. Granite ascent and emplacement during contractional deformation in convergent orogens. Journal of Structural Geology 20, 1365–1393.
Clemens, J.D., 1998. Observations on the origins and ascent mechanisms of granitic magmas. Journal of the Geological Society of London 155, 843–851.
Dahlen, F.A., 1990. Critical taper model of fold-and-thrust belts and accretionary wedges. Annual Reviews of Earth and Planetary Sciences 18, 55–99.
DeCelles, P.G., Mitra, G., 1994. History of the Sevier orogenic wedge in terms of critical taper models, Northeast Utah and Southwest Wyoming. Geological Society of America Bulletin 107, 454–462.
Duebendorfer, E.M., Chamberlain, K.R., Fry, B., 2006. Mojave-Yavapai boundary zone, southwestern United States: a rifting model for the formation of an isotopically mixed crustal boundary zone. Geology 34, 681–684.
Duebendorfer, E.M., Chamberlain, K.R., Jones, C.S., 2001. Paleoproterozoic tectonic history of the Cerbat Mountains, northwestern Arizona: implications for crustal assembly in the southwestern United States. Geological Society of America Bulletin 113, 575–590.
Eichhubl, P., Aydin, A., 2003. Ductile opening-mode fracture by pore growth and coalescence during combustion alteration of siliceous mudstone. Journal of Structural Geology 25, 121–134.
Gillespie, P.A., Howard, C.B., Walsh, J.J., Watterson, J., 1993. Measurement and characterization of spatial distributions of fractures. Tectonophysics 226, 113–141.
Gillespie, P.A., Johnston, J.D., Loriga, M.A., McCaffrey, K.J.W., Walsh, J.J., Watterson, J., 1999. Influence of layering on vein systematics in line samples. In: McCaffrey, K.J.W., Lonergan, L., Wilkinson, J.J. (Eds.), Fractures, Fluid Flow and Mineralization. Geological Society Special Publications, vol. 155, pp. 35–56.
Guernina, S., Sawyer, E.W., 2003. Large-scale melt-depletion in granulite terranes: an example from the Archean Ashuanipi Subprovince of Quebec. Journal of Metamorphic Geology 21, 181–201.
Hand, M., Dirks, P.H.G.M., 1992. The influence of deformation on the formation of axial-planar leucosomes in the segregation of small melt bodies within the migmatitic Napperby Gneiss, central Australia. Journal of Structural Geology 14, 591–604.
Hawkins, D.P., Bowring, S.A., Ilg, B.R., Karlstrom, K.E., Williams, M.L., 1996. U-Pb geochronologic constraints on the Paleoproterozoic crustal evolution of the Upper Granite Gorge, Grand Canyon, Arizona. Geological Society of America Bulletin 108, 1167–1181.
Holyoke, C.W., Rushmer, T., 2002. An experimental study of grain scale melt segregation mechanisms in two common crustal rock types. Journal of Metamorphic Geology 20, 493–512.
Ilg, B.R., Karlstrom, K.E., Hawkins, D.P., Williams, M.L., 1996. Tectonic evolution of Paleoproterozoic rocks in the Grand Canyon: insights into middle-crustal processes. Geological Society of America Bulletin 108, 1149–1166.
Jensen, H.J., 1998. Self-organized Criticality: Emergent Complex Behavior in Physical and Biological Systems. Cambridge University Press, Cambridge.
Karlstrom, K.E., Bowring, S.A., Karlstrom, K.E., 1991. Style and timing of early Proterozoic deformation in Arizona; constraints on tectonic models. In: Proterozoic Geology and Ore Deposits of Arizona. Arizona Geological Society Digest, vol. 19, pp. 1–10.
Laporte, D., Watson, E.B., 1995. Experimental and theoretical constraints on melt distribution in crustal sources; the effect of crystalline anisotropy on melt interconnectivity. Chemical Geology 124, 161–184.
Ledru, P., Courrioux, G., Lardeaux, J.M., Montel, J.M., Vanderhaeghe, O., Vitel, G., 2001. The Velay dome (French Massif Central): melt generation and granite emplacement during orogenic evolution. Tectonophysics 342, 207–237.
Loriga, M.A., 1999. Scaling systematics of vein size: an example from the Guanajuato mining district (central Mexico). In: McCaffrey, K.J.W., Lonergan, L., Wilkinson, J.J. (Eds.), Fractures, Fluid Flow and Mineralization. Geological Society, London, Special Publications, vol. 155, pp. 57–67.
Marchildon, N., Brown, M., 2001. Melt segregation in late syn-tectonic anatectic migmatites: an example from the Onawa contact aureole, Maine, USA. Physics and Chemistry of the Earth: Part A, Solid Earth and Geodesy 26, 225–229.
Marchildon, N., Brown, M., 2003. Spatial distribution of melt-bearing structures in anatectic rocks from Southern Brittany, France: implications for melt transfer at grain- to orogen-scale. Tectonophysics 364, 215–235.
Mehnert, K., 1968. Migmatites and the Origin of Granitic Rocks. Elsevier, Amsterdam.
Petford, N., Cruden, A.R., McCaffrey, K.J.W., Vigneresse, J.-L., 2000. Granite magma formation, transport and emplacement in the Earth's crust. Nature 408, 669–673.
Petford, N., Kerr, R.C., Lister, J.R., 1993. Dike transport of granitoid magmas. Geology 21, 845–848.
Platt, J.P., Vissers, R.L.M., 1980. Extensional structures in anisotropic rocks. Journal of Structural Geology 2, 397–410.
Rabinowicz, M., Vigneresse, J.-L., 2004. Melt segregation under compaction and shear channeling: application to granitic magma segregations in a continental crust. Journal of Geophysical Research 109, B04407.
Sawyer, E.W., 1994. Melt segregation in the continental crust. Geology 22, 1019–1022.
Sawyer, E.W., 2001. Melt segregation in the continental crust: distribution and movement of melt in anatectic rocks. Journal of Metamorphic Geology 19, 291–309.
Simakin, A., Talbot, C., 2001. Tectonic pumping of pervasive granitic melts. Tectonophysics 332, 387–402.
Soesoo, A., Kalda, J., Bons, P., Urtson, K., Kalm, V., 2004. Fractality in geology; a possible use of fractals in the studies of partial melting processes. Proceedings of the Estonian Academy of Sciences, Geology 53, 13–27.
Sornette, D., 2000. Critical Phenomena in Natural Sciences; Chaos, Fractals, Self Organization and Disorder: Concepts and Tools. Springer-Verlag, Berlin.
Tanner, D.C., 1999. The scale-invariant nature of migmatite from the Oberpfalz, NE Bavaria and its significance for melt transport. Tectonophysics 302, 297–305.
Turcotte, D.L., 1997. Fractals and Chaos in Geology and Geophysics. University of Cambridge, Cambridge.
Vanderhaeghe, O., 1999. Pervasive melt migration from migmatites to leucogranites in the Shuswap metamorphic core complex, Canada: control of regional deformation. Tectonophysics 312, 35–55.
Vanderhaeghe, O., 2001. Melt segregation, pervasive melt migration and magma mobility in the continental crust: the structural record from pores to orogens. Physics and Chemistry of the Earth: Part A, Solid Earth and Geodesy 26, 213–223.
Vanderhaeghe, O., 2009. Migmatites, granites, and orogeny: flow modes of partially-molten rocks and magmas associated with melt/solid segregation in orogenic belts. Tectonophysics 477, 119–134.
Van der Molen, I., 1985. Interlayer material transport during layer-normal shortening. Part 1. The Model. Tectonophysics 115, 275–295.
Vernon, R.H., Collins, W.J., 1988. Igneous microstructures in migmatites. Geology 16, 1126–1129.
Vigneresse, J.-L., Burg, J.P., 2000. Continuous vs. discontinuous melt segregation in migmatites: insights from a cellular automaton model. Terra Nova 12, 188–192.
Vigneresse, J.-L., Tikoff, B., 1999. Strain partitioning during melting and crystallizing felsic magmas. Tectonophysics 312, 117–132.
Weinberg, R.F., 1999. Mesoscale pervasive felsic magma migration: alternatives to dyking. Lithos 46, 393–410.
Weinberg, R.F., Mark, G., 2008. Magma migration, folding, and disaggregation of migmatites in the Karakoram Shear Zone, Ladakh, NW India. Geological Society of America Bulletin 120, 994–1009.
Weinberg, R.F., Mark, G., Reichardt, H., 2009. Magma ponding in the Karakoram shear zone, Ladakh, NW India. Geological Society of America Bulletin 121, 278–285.
Weinberg, R.F., Podladchikov, Y., 1994. Diapiric ascent of magmas through power law crust and mantle. Journal of Geophysical Research 99, 9543–9559.
Weinberg, R.F., Searle, M.P., 1998. The Pangong Injection Complex, Indian Karakoram: a case of pervasive granite flow through hot viscous crust. Journal of the Geological Society, London 155, 883–891.
Williams, M.L., 1991. Overview of Proterozoic metamorphism in Arizona. In: Karlstrom, K.E. (Ed.), Proterozoic Geology and Ore Deposits of Arizona. Arizona Geological Society Digest, vol. 19, pp. 11–26.
Wooden, J.L., DeWitt, D., 1991. Pb isotopic evidence for a major early crustal boundary in western Arizona. In: Karlstrom, K.E. (Ed.), Proterozoic geology and ore deposits of Arizona. Arizona Geological Society Digest, vol. 9, pp. 27–50.